

Applications of LWIR Polarimetric Video From a Low-flying Platform

Hamilton Scott Clouse and Hamid Krim and Wesam Sakla

Abstract

Polarimetric video is currently utilized for object detection and 3D inference. We demonstrate further novel analyses and applications of the polarization phenomenon. The first effort here described utilizes a physics-based model for emission polarization in the long-wave infrared band to segment the pixels in each frame into classes representing different materials in the scene. In the second effort we are able to classify human actions without performing a segmentation but, by leveraging the polarization information.

I. INTRODUCTION

Usage of video capture devices in arenas such as security has afforded an added temporal facet to traditional remote sensing. Separately, the addition of multi and hyper-spectral imaging devices have further improved the diversity, and thus the utility of the resulting data for decision making. The two ideas have recently been merged via the conjunction of video data collection in multiple wavelengths with polarimetric sensors. The resulting data is video of the traditionally collected intensity information, as well as the polarized status of the incoming radiation. An example of a current application that could possibly benefit from this extension is human activity analysis. Approaches to this problem can be characterized by the scale at which they operate. In this effort, we focus on the *actions* performed by humans, e.g. walking. This is a more coarse scale than that of *atomic-actions*, e.g. raising a foot, and finer than that of *activities*, e.g. walking to the car. In infrared video, thermal diversity may be limited to the extent that objects of interest may be indistinguishable from other elements of the scene. In such a situation, current human action classification techniques are unable to perform due to the lack of a correct segmentation. Information about the polarization of the scene adds sufficient diversity to perform such a detection/segmentation.

The first effort here described utilizes a physics-based model for emission polarization in the long-wave infrared band to segment the pixels in each frame into classes representing different materials in the scene. While this is a computationally intense process, the segmentation is useful as input to other algorithms for further processing. However, the additional polarization diversity is sufficient to perform the action classification without the detection/segmentation process.

In the second effort, we distinguish between, and classify three actions: walking, walking while carrying a heavy load, and running. By utilizing higher order statistics of the polarization diversity as features we are able to classify the actions without segmenting the human actors from the remainder of the scene.

The data used for testing was a polarimetric infrared video dataset consisting of videos of 20 individuals performing two actions (walking and walking while carrying a heavy load) in three separate instances and an eight individuals running in three separate instances (a total of 148 sample actions). Each scene was comprised of between five and ten materials. The data was captured from instrumentation mounted on a simulated low-flying platform.

The remainder of this paper is structured thus: Section II gives a brief overview of previous efforts related to our contribution, Section III describes the exploited phenomena, Section IV contains details about the sensor and resulting collected data, Section V describes the information extraction process and ensuing calculations and concluding remarks are in Section VI

II. RELATED WORK

Polarization has been of interest for many years [1], [2]. It has been utilized for modelling [3]–[5], communications [6] and many RADAR-related applications [7]–[11]. In this work, we consider the polarization of a different wavelength signal and novel applications thereof: polarimetric long-wave infrared (LWIR) video.

While much of the current work in polarimetric LWIR video focuses on the development of the sensors and post-processing methods, some application efforts have surfaced in the last few years. The detection of manmade objects [12]–[14] is of great interest due to the strong polarizing nature of manmade surfaces. Some efforts have also been made in the 3D reconstruction [15], [16] and discrimination of such objects [17], [18]. Much work has been done toward automated target detection and tracking [19]–[26]. While some efforts have utilized LWIR for human detection [27] and human action classification [28], no such efforts have, however, been made using polarimetric LWIR video.

An entire field of study, ellipsometry, centers around observing the polarization of reflections and emissions of electromagnetic waves from target materials. For reflections, the subject materials are illuminated whereas for emissions they are heated. Both the intensity and polarization states of the reflected/emitted waves are observed such that the response of the material is sampled in a hemispherical pattern centered on the subject material. By studying these observations one can discern properties of the materials, e.g. the index of refraction. Numerous physics-based parametric models [29]–[32] for electromagnetic wave emissions have been proposed and applied [33] to match the data collected through such studies. In the first work described here, we propose a means

to distinguish between materials in a scene of the micro-polarimeter video. This is accomplished by fitting one of the more recent [16] models to the observed data via the parameters. Thus, the parameters of the material that produced the data were attained.

Segmentation of images in modalities operating in parts of the spectrum outside the visible range, and the subsequent study of the corresponding response of materials in those ranges, are not new (e.g. hyperspectral remote sensing). Existing techniques, however, focus on the problem strictly as an image processing problem. We propose a novel contribution of combining the physics-based emission polarization model and the collected video data for similar applications. The difficulty of this task lies in the unknown number of materials present in the scene. Not only are the parameters of the materials composing the scene unknown, but also the number of materials. This difficulty is addressed via statistical analysis techniques in the space of parameters. With the assumption that the materials are unchanged in a single scene, it is possible to utilize all the data collected over the entire length of a single video to characterize the constituents. Once this parameter estimation is completed for the different materials in the scene, the frames are segmented by material.

The second contribution of this effort focuses on the phenomenon of human activities. We are able to distinguish between actions in different video sequences, each showing an individual performing one of several possible activities, and subsequently classify the actions. Statistical calculations for activity recognition solely based on the data have been difficult due to the variation in texture, illumination, occlusions, etc.. While we do not address occlusion in this work, we do consider texture and illumination. As in Section IV-B, data in the LWIR spectrum is benefited by the lack of shadows and slow changes in intensity. This is equivalent to circumventing the illumination problem with traditional visible spectrum observation. The issue of textural diversity is, however, still exhibited. The polarization information of the scene becomes advantageous for this obstacle. In the data collection utilized for this work, the background is a gravel lot that is stationary with respect to the observer.

The significance of this analysis also lies in exploiting a novel sensing modality: long-wave infrared (LWIR) polarimetric video. The novelty of the LWIR micro-polarimeter array is its real-time video capture of the polarization diversity of the electromagnetic waves observed in the thermal sub-band. In the past, such polarization data has only been available for still scenes captured at separate instances in time: a polarization filter was placed between the scene and the sensor, an image was collected and the filter was rotated in preparation for the next image collection. The added sequential nature afforded by the advent of video to this modality allows time-series analysis techniques to be applied. This approach proved viable for leveraging the discriminatory properties of polarization diversity for the problem, with respect to material composition and surface structure, in contrast to the traditionally complex preprocessing techniques common to video analysis.

Human action analysis, as a specific problem in remote sensing and an application of computer vision, is an important

focus of much current research [34]–[36]. While no standard definitions have been formulated, a common taxonomy utilized to distinguish between varying scopes of study is emerging.

- 1) An *action* is a simple, low-level motion such as “raising an arm” or “walking.”
- 2) *Activities* are combinations of actions, e.g. “waiting for a bus.”
- 3) An instant where multiple individuals perform a variety of activities is called an *event*, e.g. a football game.
- 4) A *behavior* is a pattern in an individual’s or group’s activities.

Many techniques and approaches have been implemented to tackle the problem of detecting, recognizing, identifying and then exploiting human action descriptions. A recent review [37] separates the approaches into two main categories: “single-layer” and “hierarchical”. The latter category contains techniques that describe human activities by examining layered deconstructions of those activities. From those deconstructions, the classification for the activity is determined. Efforts in this category can be more specifically described by the approaches they use to describe and combine the deconstructed pieces: statistics/Hidden Markov Models (HMM’s) [38], syntactic grammar organizations [39], [40] or atomic-actions/subevents [41], [42].

In contrast, the single-layer techniques directly utilize images or video to conclude the activities’ classifications. In [37], the single-layer approaches are further divided into space-time and sequential approaches. This segregation is performed via the method with which the efforts manage the temporal dimension of the data. Space-time approaches treat the temporal dimension as a third spatial dimension in that a video of an action is analyzed as a volume [43]–[46] or as local features [47]–[49] or trajectories within that volume [50]–[52]. Sequential methods abstract the input videos as sequences of measurements from which feature vectors are extracted. These features are used to classify action sequences by either updating a state model that is compared to a trained state sequence for each action [53]–[55] or by comparing them to templates of expected action sequences [56]–[58].

Due to the discrete nature of the action categories, a signature-based approach is explored to distinguish the set of all action primitives. Since the goal of this effort is to classify actions, a single-layer space-time approach is chosen over the added complexity of the hierarchical methods. Our approach, in addition to being a single-layer approach, intuitively appealing in using statistical analysis afforded by the data-type. Many current techniques require considerable preprocessing to provide suitable data on which they may operate. These preprocessing stages consist of a multitude of tasks ranging from user input such as the initial location of a subject’s extremities which in turn depend on “perfect” segmentation of the subject in each frame of an image sequence.

III. BACKGROUND

A. Polarization of EM Radiation

1) *Electromagnetic Wave Equation:* In general, an electromagnetic (EM) wave traveling in a direction ‘z’ is represented

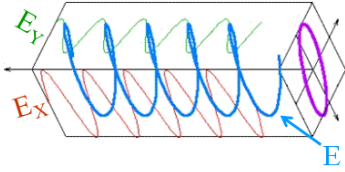


Figure 1. The E-field component of an EM wave rotates about the transverse axis and thus traces an ellipse in the plane of rotation. This wave, E , can be decomposed into orthogonal components E_X and E_Y .

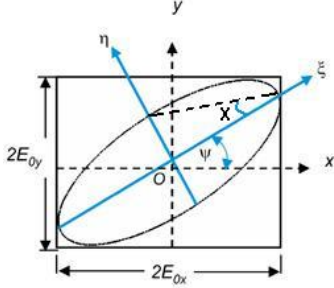


Figure 2. The polarization ellipse with the labelled parameters (From [60]). E_{0x} and E_{0y} are the amplitudes of the corresponding orthogonal constituent waves, ξ and η are the major and minor axes of the ellipse, ψ is the angle of polarization and χ is the angle of ellipticity.

by the superposition of two plane-waves also traveling in the z-direction as described by the following equation and shown in Figure 1,

$$\vec{E}(z, t) = \vec{E}_X(z, t) + \vec{E}_Y(z, t). \quad (1)$$

Following the derivation in [59], we can rewrite the constituent waves $\vec{E}_X(z, t)$ and $\vec{E}_Y(z, t)$ in terms of amplitude E_{0*} , frequency ω and phase difference δ , as in Eqs. (2) and (3), whose ratio yields an equation of an ellipse, as shown in Eq. (4), the equation of an ellipse:

$$\vec{E}_X(z, t) = \vec{i}E_{0x} \cos(kz - \omega t), \quad (2)$$

$$\vec{E}_Y(z, t) = \vec{j}E_{0y} \cos(kz - \omega t + \delta), \quad (3)$$

$$\left(\frac{E_Y}{E_{0y}}\right)^2 + \left(\frac{E_X}{E_{0x}}\right)^2 - 2\left(\frac{E_X}{E_{0x}}\right)\left(\frac{E_Y}{E_{0y}}\right)\cos(\delta) = \sin^2(\delta). \quad (4)$$

As indicated by the above equations, a propagating electromagnetic wave will have some rotation about the z-axis, and will thus trace out an ellipse (Fig.2) in the plane of rotation, as shown in Fig.1. For different values of E_{0x} , E_{0y} , and δ (the phase difference between the two orthogonal waves), the ellipse will have different shapes. There are certain states, called degenerate states, that are produced for a certain parameter value of interest, which act as a basis by which any generally polarized waveform may be completely described (Fig.(3)). That is precisely what the Stokes' vector representation exploits.

2) *Stokes' Vector Relations*: Stokes [61] proposed a convenient means to describe incoherent polarized light in the form of a vector (or a set of parameters), S . This idea was particularly novel for interpreting each parameter as a measure of the "preference" of the observed light in a certain direction of polarization. The vector comprises four entities:

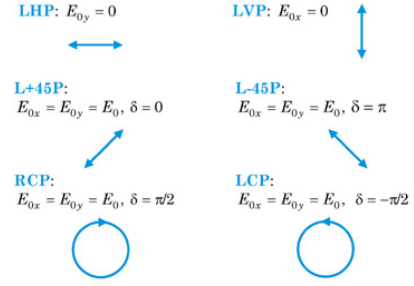


Figure 3. The degenerate states of the polarization ellipse with conditions (From [60]). E_{0x} and E_{0y} are the amplitudes of the corresponding orthogonal constituent waves, and δ is the phase difference between those waves. From top-left, proceeding clockwise: linear horizontal polarized (LHP), linear vertical polarized (LVP), linear -45° polarized (L-45P), left circular polarized (LCP), right circular polarized (RCP), linear $+45^\circ$ polarized (L+45P).

- S_0 - intensity,
- S_1 - horizontal preference,
- S_2 - $+45^\circ$ preference,
- S_3 - right circular preference.

In this formalism the intensity parameter S_0 is, for example in imaging, the gray-scale picture one would normally capture with a camera. The preference images (parameters, elements, etc.) are relations between pairs of degenerate states representing the observed light, e.g. the horizontal preference (S_1) is the difference in intensities of the horizontal (LHP) and vertical (LVP) degenerate states which characterize the observed light.

Another advantage of the Stokes' vector formalism is the ease of calculation from readily measurable phenomena. By observing light through a linear polarizing filter at various orientations, one can observe the representative degenerate states, as shown in Fig. (3), from which the Stokes' vector may be determined. These images are denoted by I_ϕ , where ϕ is the angle corresponding to the orientation of the linear polarizer's transmission, measured clockwise from the horizontal. Eqn. (5) relates the Stokes' vector representation (S) to the collected image representation (I_ϕ) and also to the orthogonal linear (E_X, E_Y) basis (where δ is the phase difference invoked in Fig.(3)):

$$S = \begin{bmatrix} S_0 \\ S_1 \\ S_2 \\ S_3 \end{bmatrix} = \begin{bmatrix} E_{0x}^2 + E_{0y}^2 \\ E_{0x}^2 - E_{0y}^2 \\ 2E_{0x}E_{0y}\cos(\delta) \\ 2E_{0x}E_{0y}\sin(\delta) \end{bmatrix} = \begin{bmatrix} \frac{1}{2}(I_0 + I_{45} + I_{90} + I_{135}) \\ I_0 - I_{90} \\ I_{45} - I_{135} \\ I_R - I_L \end{bmatrix}. \quad (5)$$

The above equations only hold true for completely polarized EM waves. Naturally occurring EM waves are, however, not completely polarized, but are partially polarized. This is tantamount to saying that they can be represented as the summation (S') of polarized (S_p) and unpolarized (S_u) components weighted by a value $\mathcal{P} \in [0, 1]$, the degree of polarization (DoP).

$$S' = (1 - \mathcal{P})S_u + \mathcal{P}S_p = (1 - \mathcal{P}) \begin{bmatrix} S_{u_0} \\ 0 \\ 0 \\ 0 \end{bmatrix} + \mathcal{P} \begin{bmatrix} S_{p_0} \\ S_{p_1} \\ S_{p_2} \\ S_{p_3} \end{bmatrix}. \quad (6)$$

Historically, two variables/features have been used to characterize and to explore the polarization phenomenon: ψ and \mathcal{P} . On one hand, the angle of polarization, ψ (Eqn. (7)), is directly observed on the polarization ellipse, on the other, the degree of polarization (DoP, \mathcal{P}) is a derived feature. In conditions lacking circular polarization, which is most often the case in passive sensing settings [62], the DoP is well approximated by the degree of linear polarization (DoLP), as shown in Eq. (8) also denoted by \mathcal{P} .

$$AoP = \psi = \frac{1}{2} \tan^{-1} \left(\frac{S_2}{S_1} \right), \quad (7)$$

$$DoLP = \mathcal{P} = \frac{\sqrt{S_1^2 + S_2^2}}{S_0}. \quad (8)$$

To promote the development of our algorithm, we employ a model of the above described physical phenomenon.

B. Physics-based Model of Emission Polarization

Observed radiance can be represented as a Stokes vector \mathbb{L} and thus related as a function of the irradiance of the object, Stokes vector \mathbb{E} , and the 4×4 Mueller matrix f , through which the irradiance is transformed:

$$\mathbb{L} = f\mathbb{E} \quad (9)$$

This f matrix is a general representation of any optical element but, in our setting, represents how the material of an object transforms the irradiance before it is observed as radiance. Such a matrix can be modeled via a bi-directional reflection distribution function (BRDF), a statistical means of describing the material of the object and its response at different wavelengths (λ), producing $f_{pBRDF}(\lambda, \theta, \phi, n, k)$. Here, the θ and ϕ are the angles representing the three-dimensional orientation of the observation with respect to the normal of the object's surface.

In [32], a polarimetric BRDF (pBRDF) model, based on the micro-facet model of Torrance and Sparrow [63], for LWIR emissions is presented. It has since been generalized in [64] to a combination of probabilistic distributions with tunable parameters.

Since the natural occurrence of circular polarization is commonly known to be negligible [62], it is only necessary to consider the unpolarized and linearly polarized components of the Stokes vectors. Additionally, in the setting of emission polarization, the irradiance from within an object is typically considered unpolarized and can be modeled as a black body irradiator. These simplifications lead to the following form:

$$\mathbb{L} = f\mathbb{E} = \begin{bmatrix} S'_0 \\ S'_1 \\ S'_2 \end{bmatrix} = \begin{bmatrix} f_{00} & f_{01} & f_{02} \\ f_{10} & f_{11} & f_{12} \\ f_{20} & f_{21} & f_{22} \end{bmatrix} \begin{bmatrix} S_0 \\ 0 \\ 0 \end{bmatrix} \quad (10)$$

where S_0 is the irradiance of the object (e.g. a function of λ and temperature for black body models) and S' is the observed radiance. From the pBRDF models, the components of f can be manipulated to produce a model for \mathcal{P} , denoted $\hat{\mathcal{P}}$, mapping the parameters of the component distributions to an estimate of \mathcal{P} . It is this model estimate, $\hat{\mathcal{P}}(\theta_v(\theta, \phi), n, k)$, that we utilize (Eqn. 11), as derived in [65].

$$\hat{\mathcal{P}} = \frac{2A \sin^2(\theta_v) \cos(\theta_v)}{A^2 \cos^2(\theta_v) + \sin^4(\theta_v) + B^2 \cos^2(\theta_v)}, \quad (11)$$

where the functions A and B are defined in terms of the function $\theta_v(\theta, \phi)$ as follows:

$$A(n, k, \theta_v) = \sqrt{\frac{\sqrt{C} + D}{2}}, \quad (12)$$

$$B(n, k, \theta_v) = \sqrt{\frac{\sqrt{C} - D}{2}}, \quad (13)$$

$$C(n, k, \theta_v) = 4n^2 k^2 + D^2, \text{ and} \quad (14)$$

$$D(n, k, \theta_v) = n^2 - k^2 - \sin^2(\theta_v). \quad (15)$$

From this representation of $\hat{\mathcal{P}}$, given a sufficient sampling of \mathcal{P} , we can compute candidate values for n and k to distinguish between materials in a scene.

C. Statistical Analysis Tools

Here we briefly cover some rudimentary statistics utilized in a portion of this work.

Consider a vector $\mathbf{x} \in \mathbb{R}^n$ of n samples x_i , $i \in [1, n]$, from a continuous random variable $x \in \mathbb{R}$. One alternative approach to describing a probability distribution function $f(x)$ of x is via its statistical moments. These moments quantitatively describe the shape of a distribution so as to facilitate its classification and identification. The k^{th} moment of the function $f(x)$ centered about the value c is described by Eq. (16),

$$\mu_k = \int_{-\infty}^{\infty} (x - c)^k f(x) dx. \quad (16)$$

The mean, or expected value $\mu = E[x]$, of a random variable can be described as the first moment of the distribution centered about zero. Moments centered about the mean of the variable are called ‘‘central moments’’. This makes the central moments dependent only on the shape and scale of the distribution. Of particular focus in this effort are standardized, central moments that have been normalized by the k^{th} power of the variance σ . Here, again, a level of invariance is added to the moments, in that standardized moments are strictly influenced by the shape of the distribution, and not on the location or scale. Commonly, in conjunction with the mean and the variance, the third and fourth standardized moments (the skewness and kurtosis, respectively) are also considered to describe a distribution (shown as calculated),

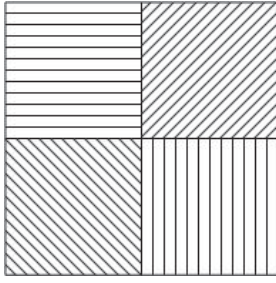


Figure 4. Superpixel polarizing filter pattern of micro-polarimeter focal-plane array. Starting at the top left and proceeding clockwise, the orientations are 0° , $+45^\circ$, 90° and -45° .

$$\text{Skew}(x) = \frac{\frac{1}{n} \sum_{i=1}^n (x_i - \mu)^3}{\left(\frac{1}{n} \sum_{i=1}^n (x_i - \mu)^2 \right)^{\frac{3}{2}}}, \quad (17)$$

$$\text{Kurt}(x) = \frac{\frac{1}{n} \sum_{i=1}^n (x_i - \mu)^4}{\left(\frac{1}{n} \sum_{i=1}^n (x_i - \mu)^2 \right)^2}. \quad (18)$$

While these two descriptors seem similar, the difference in the exponent is key to the difference in describing the shape of the distribution. The skewness of a distribution is a measure of the asymmetry of that distribution and the kurtosis of a distribution describes its peakedness. So, for the random vector \mathbf{x}_i , these moments describe the shape of the distribution of the random variable x .

The combination of these higher order statistics with the location and spread information contained in the mean and variance, respectively, provide a good description of a distribution, and allow for a significant comparison between distributions.

IV. DATA DESCRIPTION

A. Data Collection and Characteristics

The instrument by which the data used in this work was captured produces video sequences of the Stokes [61] vector of a scene. The video is in three channels, much like the three color channels of a CCD camera:

- S_0 - intensity,
- $\mathcal{P}S_1$ - horizontal preference,
- $\mathcal{P}S_2$ - $+45^\circ$ preference.

The data utilized in this work is the result of a post-processing method applied to an output from a cooled micro-polarimeter focal plane array (FPA). Each cluster of four pixels on the FPA forms a ‘‘super-pixel,’’ as depicted in Fig.(4). The patterns indicate the orientation of a linear polarizing filter placed over each sensor in a pattern reminiscent of the Bayer filter pattern used for color CCD cameras.

The raw output from these sensors is a four-channel (one for each I_ϕ from Section III-A2) image sequence. For each image

Sub-bands of the Infrared (IR) Spectrum	
Band Label	Wavelength (λ) Range
Near infrared (NIR)	$0.7 - 1\mu m$
Short-wave infrared (SWIR)	$1 - 3\mu m$
Mid-wave infrared (MWIR)	$3 - 5\mu m$
Long-wave infrared (LWIR)	$8 - 14\mu m$

Table I
RANGES OF THE DEFINED SUB-BANDS WITHIN THE IR SPECTRUM BAND.

in the sequence, these channels are combined and processed, as described in [66], to produce a video sequence with three channels, one for each Stokes component, and hence the data analyzed in this work. Each frame is 471×641 pixels in size, and the video is captured at twenty-four frames per second (24 fps), resulting in each sequence spanning approximately 1500 frames. The target wavelength of the sensor is the LWIR spectrum ($8-14\mu m$), i.e. the thermal spectrum. Subjects in the dataset performed three activities along a predefined course: walking, walking while carrying a heavy bag and running. The resulting scenes consist of a gravel lot across which each action is performed, progressing from the right to the left extents of the field of view (fov) of the sensor.

B. Infrared Band Implications

In Sect.III-A our discussion did not focus on any specific band of the EM spectrum, though some intuition from visible light was called upon in the given examples. The formalism is indeed applicable to all frequency ranges of the EM spectrum. In remote sensing, diversity of modalities is a necessity, and here we focus on an imaging type that caters to such a requirement. Imaging in the infrared band is useful for observation in low-light conditions since IR sensors, in spite of their relatively small band and collection of relatively few photons, are very accurate. With proper scaling, they afford object discernment under a greater range of operating conditions than does visible light imaging [67]. As described in Table I, there are several sub-bands defined within the infrared band ($\lambda \in [0.7, 14]\mu m$).

These different bands are defined by the bandwidth that different sensor types cover, e.g. NIR is from the end of perception by the human eye through the response of silicon based detectors [68]. Our work focuses on the LWIR band. As can be seen in Fig.5, reflections dominate all the IR bands, as in the visible light spectrum, except for the LWIR band. In the LWIR band emitted radiation is dominant, i.e. thermal emissions. The advantage of imaging in this band is that heat/radiation sources are themselves observed, and small sources are not so obstructed by the reflections/shadows from larger/stronger sources, e.g. the sun, as they would be in other bands. While this may cause some problems, e.g. there are multiple sources instead of one strong one (e.g. the sun in the visible sub-band), it simplifies many calculations since it is not necessary to take into account reflections and shadows in the presence of moving objects in a scene. There is not a total absence of shadows and reflections and these can cause ambiguities in thermal equilibrium conditions, but because heat transfer is a relatively slow process compared with visible light transmittance, and with video capture rates,

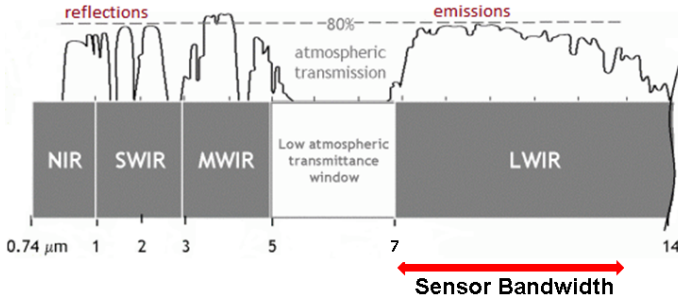


Figure 5. The Infrared band of the EM spectrum with radiance curves for reflections and thermal emissions. Emissions clearly dominate the spectrum in the LWIR (From [69]).

they are negligible over short time intervals.

V. EXPERIMENTS AND RESULTS

A. Material Segmentation

It is well known that the DoLP of a given object of a given material can be represented as a function of the view angle with respect to the normal of the surface [70]. Assuming a sensor that is stationary with respect to the background of the scene, the motion of the objects in the scene will induce changes in the observed DoLP peculiar to those objects' structures and materials. We can represent this relationship accurately with the following equation:

$$\frac{\partial \mathcal{P}}{\partial t} = \frac{\partial \mathcal{P}}{\partial \theta} \frac{\partial \theta}{\partial t} \quad (19)$$

This relation captures the well-established correspondence between the DoLP of a material and the view angle. It also includes the dependence of the change in view angle on the motion observed in the video by describing the view angle as a function of time, $\theta(t)$. Abstracting a video sequence as a space-time volume and considering the values of all its voxels simultaneously allow one to derive a relative distinction between moving objects in the scene from their material properties. This is due to the video capture resulting in, effectively, a sampling of multiple $\mathcal{P}(\theta)$ curves, one for each material, at different view angles, θ . Figure 8 is a plot of each pixel measurement in such a space-time volume as observed in the data. While the peak at zero for $\frac{\partial \mathcal{P}}{\partial t}$ is dominant due to the small size of movers in the scene, the other lobes correspond to different materials in the scene, indicating that distinction is viable. To demonstrate this, we employ the previously-described physics-based model, Eqn 11 from Section III-B, to simpler but real measurements.

The data utilized for this portion of our experiments are samples from two measured $\mathcal{P}(\theta)$ curves, one for Uranium glass and one for Tungsten (Fig. 6). A separate monotonic sampling in θ was devised for each material to mimic a smooth rotation in view. Gaussian noise was added to those sampled points to produce data (Fig. 7) similar to that observed from the collected video (Fig. 8).

1) *Parameter Estimation*: For each voxel x_i in the data, we fit the model given in Eqn. 11 (sweeping through θ), to the points in its surrounding neighborhood $\mathcal{N}(x_i) = \{x_j | d(x_i, x_j) < \epsilon\}$ where $d(x_i, x_j) = \|x_i - x_j\|_2$ is the

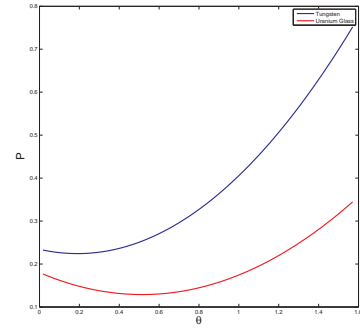


Figure 6. $\mathcal{P}(\theta)$ curves for Uranium glass (shown in red) and Tungsten (shown in blue)

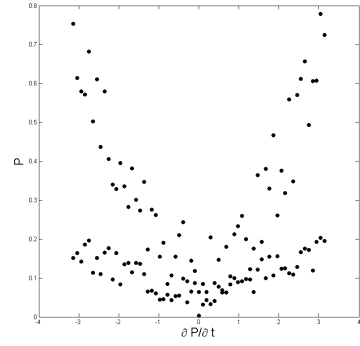


Figure 7. Scatter plot of data resulting from sampling $\mathcal{P}(\theta)$ curves for Uranium glass and Tungsten and the addition of Gaussian noise.

Euclidean distance between the points x_i and x_j in the space $\mathcal{P} \times \frac{\partial \mathcal{P}}{\partial t}$. The Nelder-Mead simplex direct search method for solving nonlinear optimization problems was employed for this fitting [71]. The value for ϵ was chosen so that in the most dense regions, few points populated each neighborhood, so as to improve the performance (speed) of the optimization. This procedure was iterated over many neighborhoods until all the voxels had been considered. The result was a set of points, one for each neighborhood, in the $n \times k$ parameter space, as

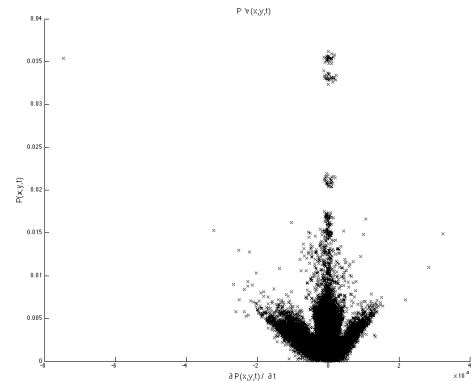


Figure 8. All DoLP measurements in a given space-time volume as a function of the partial derivative, with respect to time (frame).

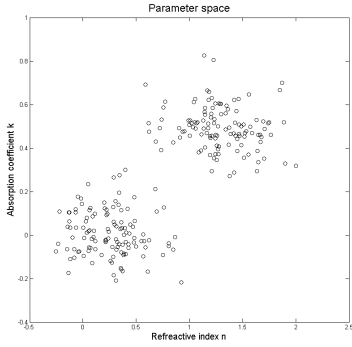


Figure 9. Points in the $n \times k$ parameter space with two clusters evident.

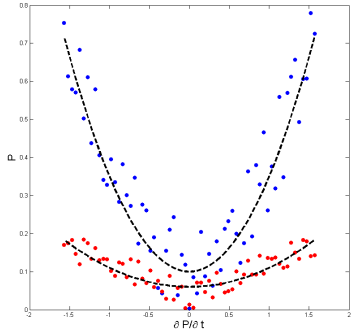


Figure 10. Material curves resulting from using cluster centers as parameter values. Data points colored to indicate true material-type (Uranium glass as red and Tungsten as blue).

shown in Fig. 9.

A hierarchical clustering was then performed in the $n \times k$ space to determine the number of clusters and their centers. The corresponding parameter values for these centers were used as the representative parameters for each voxel within a cluster. In this fashion, each voxel was categorized via material composition. Figure 10 depicts the result of such a process. The dashed lines indicate the material curves from the model $\hat{\mathcal{P}}$ when the cluster centers were utilized as parameter values. The data points are colored to indicate the material from which they were sampled.

2) *Turbo Estimation Error Correction*: Clearly, from Fig. 10, if one were to classify the data points via which model material curve they were nearest, some errors would be incurred. However, some information present in the data, omitted from the discussion in Section V-A but, included in Eqn. 19 is yet to be utilized: the time-ordering of the samples, i.e. θ 's dependence on time.

Each voxel represented in the scatter plots has a corresponding time at which it was observed. Drawing inspiration from the Turbo principle, we utilize information available that hasn't been employed, to improve the estimate (classification result) already computed. In this case, for points classified as the same material, a simple evaluation of the smoothness in the corresponding θ trajectories is sufficient to improve the classification result.

For each set of points $C^m = \{c_i^m\}$ in the data classified

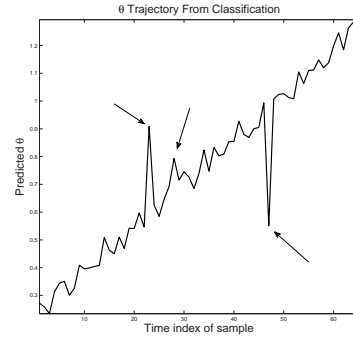


Figure 11. Resulting θ trajectory from similarly classified data points. Arrows indicate errors in the classification indicated by marked deviations from the otherwise “smooth” trajectory.

as the same material ω_m , we consider the time at which each point was sampled, t_i . Using the model curve produced from the earlier classification and the corresponding parameters (n , k and measured \mathcal{P}), we perform the inverse calculation of θ corresponding to each point. Observing the trajectory of this ordered sweep through θ , a smoothness criteria was implemented to indicate errors in the classification:

$$\left| \frac{\partial \theta}{\partial t} \right| < \delta \quad (20)$$

The current method for choosing the parameter δ is empirically based on the observed data. However, more sophisticated methods are being developed based on models of the actions to be observed in practice.

For the values of $\frac{\partial \theta}{\partial t}$ that do not meet this criteria, they are considered errors in classification and are compared to the θ -trajectories of the other material classes for proper classification.

B. Action Classification

For the experiments described below, the DoLP portion of the collected data was utilized. This data was produced following the computation given in Eqn. 8.

We represent each image sequence as a matrix $\mathbf{X} = \{x_i^j\}$ where $i \in [1, 471 \times 641]$ is the pixel index for each frame and $j \in [1, 250]$ is the frame index. For each time instant j , we calculate the mean, variance, skewness and kurtosis of the sample vector \mathbf{x}^j to produce a time series of each statistic. The result is a collection of four corresponding time series for each scenario performed by each subject.

1) *Simulations*: To validate the idea that the statistics of the frames would follow some periodicity induced by the subject action in the video, the experiment was performed with simulated data. This surrogate data consisted of video of the same frame size and rate as the collected data, and also contained sequences of single individuals performing simple actions. The notable difference between the simulated data and the collected data is the binary nature of the simulated data. Whereas the collected data pixel values are measurements from the scene, the pixel values of the simulated data are either one (1) or zero (0), corresponding to pixels that belong to the foreground and background of the scene, respectively.

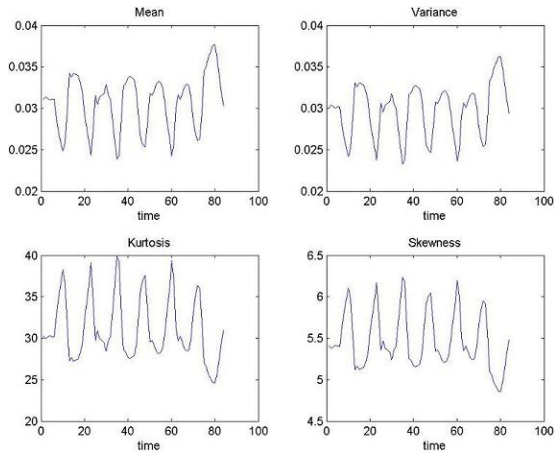


Figure 12. Higher order statistical moments for each frame of a section of the walking simulation.

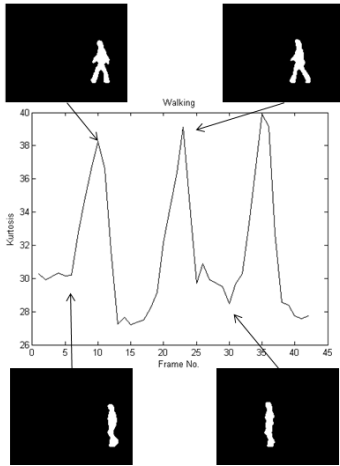


Figure 13. Correspondence between frames of the simulated walking video and the kurtosis value in each frame.

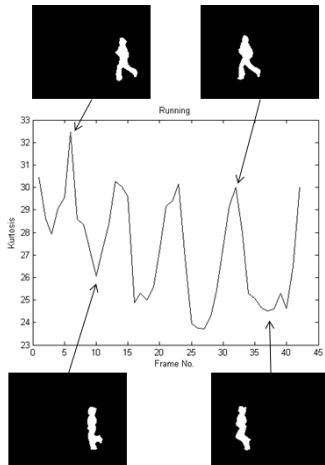


Figure 14. Correspondence between frames of the simulated running video and the kurtosis value in each frame.

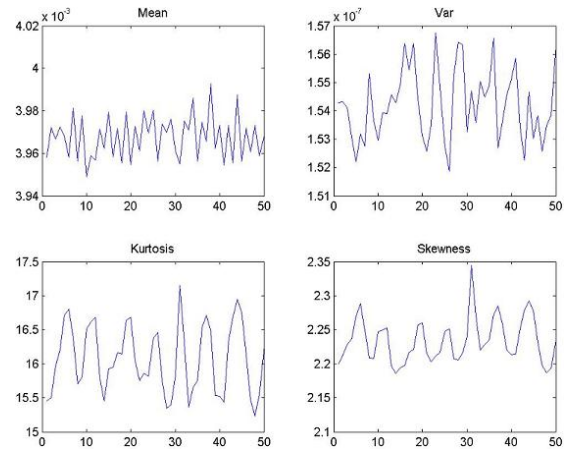


Figure 15. Representative higher order statistical moments for each frame of a section of the collected data.

The computed time-series of the statistics, shown in Fig. 12, indicates that the statistical moments of each frame vary periodically, just as the action in the videos are periodic in nature. To further explore this correlation, a qualitative frame-by-frame matching was performed (Fig.s 13 & 14), and it was subsequently determined that the periodicity of the statistics was induced by the motion in the video, as was expected from a binary video sequence.

In the binary setting, the statistics are determined by the variation in the number of foreground/background pixels. The frequencies of these values in a single frame are the direct results of the pose of the subject with respect to the viewing orientation of the camera. The performed action performed dictates the statistics of the frame.

2) *Data Exploitation:* The same computations were performed with the collected data with the simulated data. Figure 15 is representative of the statistics calculated for an action sequence from the collected dataset. The noteworthy difference between the statistics of the collected data and the simulated data is that the *mean* and *variance* of the frames of the collected data do not only not follow the periodicity of the actions, but the magnitude and variations are so slight as they can be attributed to noise. Also evident from Fig. 15 is the close correlation between the kurtosis and the skewness time-series of the representative action. Due to this extended similarity and the added variation/magnitude afforded, the kurtosis time-series was chosen as a characteristic measure of the data. Using the kurtosis time-series as a description of the action for each trial (one individual, one action), the classification was performed in a supervised learning fashion. Figure 16 shows the kurtosis time-series for the three different actions as performed by a single individual, indicating a different periodicity for each action.

The spectra of each time-series was computed and used as the feature vector for classifying the actions. To focus on the utility of these features in classifying the actions, a standard classifier was used: K Nearest Neighbors (KNN). Due to the relatively few trials available in the dataset, the leave-one-out (LOO) method was used for training/testing. The

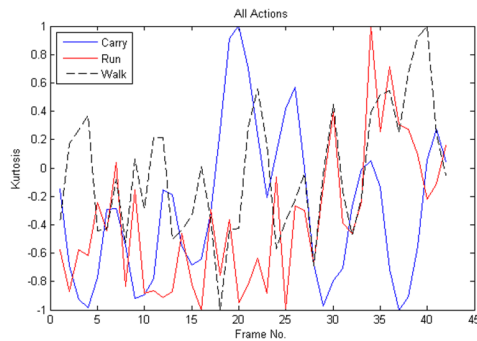


Figure 16. Kurtosis time-series sections for all actions as performed by the same individual.

Experiment	Actual		
	Walk	Carry	Run
Walk	97	3	0
Carry	0	74	26
Run	0	4	96

Table II

CONFUSION MATRIX REPRESENTING THE ACCURACY OF THE CLASSIFICATION PERFORMED (IN %) VIA THE SPECTRA OF THE KURTOSIS TIME-SERIES CHARACTERISTICS.

classifier results are displayed as a confusion matrix in Table II. The errors of classifying the “carry” action as “running” is due to the use of the spectra of the time-series as a feature for classification. The additional motion of the load created higher frequency components in the spectra, thus increasing the similarity between the spectra for “carry” and “running.”

VI. CONCLUSION & FUTURE WORK

By utilizing the LWIR polarimetric video, we’re able to capitalize on physical phenomena not previously exploited for material distinction and human action classification. While this is a first step in a new direction for applications of this modality, the results appear promising. Further effort must be applied to considering the performance of these techniques as compared with currently employed methods. For instance, a comparison of the material distinction power of polarimetric LWIR (PolarLWIR) imagery versus hyperspectral imagery (HSI) should be performed. It is expected that, while the HSI should prove more accurate in material identification, the PolarLWIR result could be sufficient in many settings and with a decreased sensor/processing cost. Also the simplicity of the calculations required for the action classification to produce such results as indicated in Table II, merits further study of similar applications.

Acknowledgements

The authors would like to thank Mrs. Olga Mendoza-Schrock, Mr. Bob Mack and Mr. Ed Zelnio of the AFRL/Sensors Directorate for their assistance, support, and guidance of this work. They would also like to thank Dr. Dan LeMaster for his continuing aid in furthering our understanding of polarization and EM physics. Additionally, they would like to thank Dr. Harish Chintakunta of North Carolina State

University for his assistance with the application of turbo error correction.

REFERENCES

- [1] R. E. Taylor, “Satellite tracking simultaneous-lobing monopulse receiving system with polarization diversity capability,” *Aerospace and Electronic Systems, IEEE Transactions on*, vol. AES-3, no. 4, pp. 664–680, 1967.
- [2] T. Barnard, J. Wasserman, and J. Schroeder, “Remote attitude sensing with polarization-modulated light,” *Aerospace and Electronic Systems, IEEE Transactions on*, vol. AES-8, no. 2, pp. 156–160, 1972.
- [3] G. Ioannidis, “Model for spectral and polarization characteristics of chaff,” *Aerospace and Electronic Systems, IEEE Transactions on*, vol. AES-15, no. 5, pp. 723–726, 1979.
- [4] R. Luebbers, V. Ungvichian, and L. Mitchell, “Gtd terrain reflection model applied to its glide scope,” *Aerospace and Electronic Systems, IEEE Transactions on*, vol. AES-18, no. 1, pp. 11–20, 1982.
- [5] T. Crimmins and W. Brown, “Image algebra and automatic shape recognition,” *Aerospace and Electronic Systems, IEEE Transactions on*, vol. AES-21, no. 1, pp. 60–69, 1985.
- [6] H. Lu, “Polarization separation by an adaptive filter,” *Aerospace and Electronic Systems, IEEE Transactions on*, vol. AES-9, no. 6, pp. 954–956, 1973.
- [7] A. Monakov, “Estimation of the covariance matrix for dependent signal samples: polarization diversity systems,” *Aerospace and Electronic Systems, IEEE Transactions on*, vol. 30, no. 2, pp. 484–492, 1994.
- [8] R. Raghavan, N. Pulsone, and D. McLaughlin, “Adaptive estimation of the polarization of a signal,” *Aerospace and Electronic Systems, IEEE Transactions on*, vol. 31, no. 2, pp. 845–852, 1995.
- [9] E. Conte and G. Ricci, “Sensitivity study of glrt detection in compound-gaussian clutter,” *Aerospace and Electronic Systems, IEEE Transactions on*, vol. 34, no. 1, pp. 308–316, 1998.
- [10] D. Garren, A. Odom, M. Osborn, J. S. Goldstein, S. Pillai, and J. Guerci, “Full-polarization matched-illumination for target detection and identification,” *Aerospace and Electronic Systems, IEEE Transactions on*, vol. 38, no. 3, pp. 824–837, 2002.
- [11] A. De Maio, G. Alfano, and E. Conte, “Polarization diversity detection in compound-gaussian clutter,” *Aerospace and Electronic Systems, IEEE Transactions on*, vol. 40, no. 1, pp. 114–131, 2004.
- [12] F. Sadjadi and C. Chun, “Passive polarimetric ir target classification,” *Aerospace and Electronic Systems, IEEE Transactions on*, vol. 37, no. 2, pp. 740–751, 2001.
- [13] F. Cremer, W. de Jong, and K. Schutte, “Infrared polarization measurements and modeling applied to surface-laid antipersonnel landmines,” 2002.
- [14] B. M. Ratliff, Villeneuve, Weinheimer, D. A. LeMaster, Mack, and Middelendorf, “Detection and tracking of rc model aircraft in lwir microgrid polarimeter data,” in *Proc. SPIE 8160, 816002 (2011)*, 2011.
- [15] R. B. Reid, M. E. Oxley, M. T. Eismann, and M. E. Goda, “Quantifying surface normal estimation,” *Polarization: Measurement, Analysis, and Remote Sensing VII*, vol. 6240, p. 624001, 2006.
- [16] M. Gartley, P. Erbach, and L. Pezzaniti, “Pose estimation of unresolved targets using polarimetric imaging,” in *Proceedings of SPIE*, ser. Polarization: Measurement, Analysis, and Remote Sensing IX, D. B. Chenault and D. H. Goldstein, Eds., vol. 7672, 2010.
- [17] Connor, Carrie, Craig, and Parsons, “Discriminative imaging using a lwir polarimeter,” *Electro-Optical and Infrared Systems: Technology and Application V*, vol. 7113, p. 71130, 2008.
- [18] A. El-Saba and W. A. Sakla, “Linear high-boost fusion of stokes vector imagery for effective discrimination and recognition of real targets in the presence of multiple identical decoys,” in *Proceedings of SPIE*, ser. Polarization: Measurement, Analysis, and Remote Sensing IX, D. B. Chenault and D. H. Goldstein, Eds., vol. 7672, 2010.
- [19] J. K. McWilliams and M. D. Srinath, “Performance analysis of a target detection system using infrared imagery,” *Aerospace and Electronic Systems, IEEE Transactions on*, vol. AES-20, no. 1, pp. 38–49, 1984.
- [20] Y. Bar-Shalom, H. Shertukde, and K. Pattipati, “Use of measurements from an imaging sensor for precision target tracking,” *Aerospace and Electronic Systems, IEEE Transactions on*, vol. 25, no. 6, pp. 863–872, 1989.
- [21] S. Blackman, R. Dempster, and T. Broida, “Multiple hypothesis track confirmation for infrared surveillance systems,” *Aerospace and Electronic Systems, IEEE Transactions on*, vol. 29, no. 3, pp. 810–824, 1993.

- [22] P. Maybeck, T. Herrera, and R. Evans, "Target tracking using infrared measurements and laser illumination," *Aerospace and Electronic Systems, IEEE Transactions on*, vol. 30, no. 3, pp. 758–768, 1994.
- [23] Y. Xiong, J.-X. Peng, M. Ding, and D.-H. Xue, "An extended track-before-detect algorithm for infrared target detection," *Aerospace and Electronic Systems, IEEE Transactions on*, vol. 33, no. 3, pp. 1087–1092, 1997.
- [24] K. Anderson and R. Iltis, "A tracking algorithm for infrared images based on reduced sufficient statistics," *Aerospace and Electronic Systems, IEEE Transactions on*, vol. 33, no. 2, pp. 464–472, 1997.
- [25] T. Meitzler, G. Gerhart, E. Sohn, and H. Singh, "Detection probability using relative clutter in infrared images," *Aerospace and Electronic Systems, IEEE Transactions on*, vol. 34, no. 3, pp. 955–962, 1998.
- [26] F. Li and X. Xu, "Modeling time-evolving infrared characteristics for space objects with micromotions," *Aerospace and Electronic Systems, IEEE Transactions on*, vol. 48, no. 4, pp. 3567–3577, 2012.
- [27] G. Aviram and S. R. Rotman, "Evaluation of human detection performance of targets embedded in natural and enhanced infrared images using image metrics," in *Opt. Eng.*, 39, 885 (2000), 2000.
- [28] J. Han and B. Bhanu, "Human activity recognition in thermal infrared imagery," in *Computer Vision and Pattern Recognition - Workshops, 2005. CVPR Workshops. IEEE Computer Society Conference on*, june 2005, p. 17.
- [29] X. D. He, K. E. Torrance, F. X. Sillion, and D. P. Greenberg, "A comprehensive physical model for light reflection," *SIGGRAPH Comput. Graph.*, vol. 25, no. 4, pp. 175–186, Jul. 1991. [Online]. Available: <http://doi.acm.org/10.1145/127719.122738>
- [30] D. D. Duncan, D. V. Hahn, and M. E. Thomas, "Physics-based polarimetric brdf models," in *Proc. SPIE 5192, Optical Diagnostic Methods for Inorganic Materials III*, vol. 129, 2003, pp. 129–140. [Online]. Available: + <http://dx.doi.org/10.1117/12.507317>
- [31] J. A. Conant and F. J. Iannarilli, Jr., "Development of a combined bidirectional reflectance and directional emittance model for polarization modeling," in *Proc. SPIE 4481, Polarization Analysis and Measurement IV*, vol. 206, 2002, pp. 206–215. [Online]. Available: + <http://dx.doi.org/10.1117/12.452890>
- [32] M. P. Fetrow, D. L. Wellems, S. H. Sposato, K. P. Bishop, T. R. Caudill, M. L. Davis, and E. R. Simrell, "Results of a new polarization simulation," in *Proceedings of SPIE*, ser. Polarization: Analysis, Measurement, and Remote Sensing IV, D. H. Goldstein, D. B. Chenault, W. Egan, and M. Duggins, Eds., vol. 4481, 2002, pp. 149–162.
- [33] F. A. Sadjadi, "Passive three-dimensional imaging using polarimetric diversity," *Optics Letters*, vol. 32, no. 3, pp. 229–231, 2007.
- [34] M. Bergonzio, S. Gong, and T. Xiang, "Recognizing action as clouds of space-time interest points," in *IEEE Conference on Computer Vision and Pattern Recognition*, 2009.
- [35] M. S. Ryoo and J. K. Aggarwal, "Semantic representation and recognition of continued and recursive human activities," *International Journal of Computer Vision*, vol. 32, pp. 1–24, 2009.
- [36] Z. Li, Y. Fu, T. S. Huang, and S. Yan, "Real-time human action recognition by luminance field trajectory analysis," in *ACM International Conference on Multimedia*, 2008.
- [37] J. K. Aggarwal and M. S. Ryoo, "Human activity analysis: A review," *ACM Comput. Surv.* 43, vol. 3, no. 16, 2011.
- [38] N. Oliver, E. Horvitz, and A. Garg, "Layered representations for human activity recognition," in *IEEE International Conference on Multimodal Interfaces*, 2002.
- [39] Y. A. Ivanov and A. F. Bobick, "Recognition of visual activities and interactions by stochastic parsing," *IEEE Transactions on Pattern Analysis and Machine Intelligence*, vol. 22, pp. 831–843, 2000.
- [40] J. S. W. and R. Chellappa, "Attribute grammar-based event recognition and anomaly detection," in *IEEE Conference on Computer Vision and Pattern Recognition Workshop*, 2006.
- [41] J. F. Allen, "Maintaining knowledge about temporal intervals," *Communications of the ACM*, vol. 26, pp. 832–843, 1983.
- [42] A. Gupta, P. Srinivasan, J. Shi, and L. S. Davis, "Understanding videos, constructing plots learning a visually grounded storyline model from annotated videos," in *IEEE Conference on Computer Vision and Pattern Recognition*, 2009.
- [43] A. F. Bobick and J. Davis, "The recognition of human movement using temporal templates," *IEEE Transaction on Patt.*, vol. 23, pp. 257–267, 2001.
- [44] E. Shechtman and M. Irani, "Space-time behavior based correlation," in *IEEE Conference on Computer Vision and Pattern Recognition*, 2005.
- [45] Y. Ke, R. Sukthankar, and M. Hebert, "Spatio-temporal shape and flow correlation for action recognition," in *IEEE Conference on Computer Vision and Pattern Recognition*, 2007.
- [46] M. D. Rodriguez, J. Ahmed, and M. Shah, "Action mach: A spatio-temporal maximum average correlation height filter for action recognition," in *IEEE Conference on Computer Vision and Pattern Recognition*, 2008.
- [47] A. Yilmaz and M. Shah, "Actions sketch: a novel action representation," in *Computer Vision and Pattern Recognition, 2005. CVPR 2005. IEEE Computer Society Conference on*, 2005.
- [48] J. C. Niebles, H. Wang, and L. Fei-fei, "Unsupervised learning of human action categories using spatial-temporal words," in *In Proc. BMVC*, 2006.
- [49] S. Savarese, A. DelPozo, J. C. Niebles, and L. F. fei, "Spatial-temporal correlations for unsupervised action classification," in *IEEE Workshop on Motion and Video Computing*, 2008.
- [50] L. W. Campbell and A. F. Bobick, "Recognition of human body motion using phase space constraints," in *IEEE International Conference on Computer Vision*, 1995.
- [51] C. Rao and M. Shah, "View-invariance in action recognition," in *IEEE Conference on Computer Vision and Pattern Recognition*, 2001.
- [52] Y. Sheikh and M. Sheikh, "Exploring the space of a human action," *Computer Vision, 2005. ICCV*, pp. 1–6, 2005. [Online]. Available: http://ieeexplore.ieee.org/xpls/abs_all.jsp?arnumber=1541250
- [53] J. Yamato, J. Ohya, and K. Ishii, "Recognizing human action in time-sequential images using hidden markov model," in *Computer Vision and Pattern Recognition, 1992. Proceedings CVPR '92., 1992 IEEE Computer Society Conference on*, 1992.
- [54] N. Oliver, B. Rosario, and A. Pentland, "A bayesian computer vision system for modeling human interactions," *Pattern Analysis and Machine Intelligence, IEEE Transactions on*, vol. 22, pp. 831–843, 2000.
- [55] F. Lv and R. Nevatia, "Single view human action recognition using key pose matching and viterbi path searching," in *Computer Vision and Pattern Recognition, 2007. CVPR '07. IEEE Conference on*, 2007.
- [56] D. M. Gavrilu and L. S. Davis, "Towards 3-d model-based tracking and recognition of human movement: a multi-view approach," in *In International Workshop on Automatic Face- and Gesture-Recognition. IEEE Computer Society*, 1995.
- [57] A. A. Efros, A. C. Berg, G. Mori, and J. Malik, "Recognizing action at a distance," in *Ninth IEEE International Conference on Computer Vision (ICCV'03) - Volume 2*, 2003.
- [58] A. Veeraraghavan, R. Chellappa, and A. Roy-Chowdhury, "The function space of an activity," in *Computer Vision and Pattern Recognition, 2006 IEEE Computer Society Conference on*, 2006.
- [59] E. Hecht, *Optics*, 4th ed., A. Black, Ed. Pearson Education, Inc., 2002.
- [60] E. Collett, *Field Guide to Polarization*, J. E. Greivenkamp, Ed. SPIE Press, 2005.
- [61] G. G. Stokes, "On the composition and resolution of streams of polarized light from different sources," *Transactions of the Cambridge Philosophical Society*, vol. 9, pp. 399–416, 1852.
- [62] J. R. Schott, *Fundamentals of Polarimetric Remote Sensing*, ser. Tutorial Texts in Optical Engineering, Unknown, Ed. SPIE Press, 2009, vol. TT81.
- [63] K. E. Torrance and E. M. Sparrow, "Theory for off-specular reflection from roughened surfaces," *Journal of the Optical Society of America*, vol. 57, no. 9, pp. 1105–1114, September 1967.
- [64] M. G. Gartley, "Polarimetric modeling of remotely sensed scenes in the thermal infrared," Ph.D. dissertation, Rochester Institute of Technology, 2007.
- [65] T. V. T. Krishna, "Exploiting passive polarimetric imagery for remote sensing applications," Ph.D. dissertation, New Mexico State University, 2008.
- [66] D. A. LeMaster and S. C. Cain, "Multichannel blind deconvolution of polarimetric imagery," *Journal of Optical Society of America*, vol. 25, no. 9, pp. 2170–2176, 2008.
- [67] T. Rogne, S. Stewart, and M. Metzler, "Infrared polarimetry: What, why, how, and the way ahead," ERIM International, Inc. and ISCIENCES, L.L.C., Tech. Rep., October 1998.
- [68] J. L. Miller, *Principles of Infrared Technology: A Practical Guide to the State of the Art*. Van Nostrand Reinhold, 1994.
- [69] C. Ibarra-Castaneda, "Quantitative subsurface defect evaluation by pulsed phase thermography: depth retrieval with the phase," Ph.D. dissertation, Laval University, 2005.
- [70] L. B. Wolff, A. Lundberg, and R. Tang, "Thermal emission polarization," in *Proceedings of SPIE*, ser. Polarization: Measurement, Analysis, and Remote Sensing II, 1999, pp. 75–86.
- [71] J. C. Lagarias, J. A. Reeds, M. H. Wright, and P. E. Wright, "Convergence properties of the nelder-mead simplex method in low dimensions," *SIAM Journal of Optimization*, vol. 9, pp. 112–147, 1998.